Probabilities for M-shell ionization in intermediate-velocity collisions of medium-mass atoms with $^4\text{He}^{2+}$ ions

Ch. Herren, B. Boschung, J.-Cl. Dousse, B. Galley, J. Hoszowska, J. Kern, and Ch. Rhême
Physics Department, University of Fribourg, CH-1700 Fribourg, Switzerland

M. Polasik
Institute of Chemistry, Nicolas Copernicus University, 87-100 Toruń, Poland

T. Ludziejewski, P. Rymuza, and Z. Sujkowski
Institute for Nuclear Studies, 05-400 Świerk, Poland

High-resolution measurements of the $K\beta_2$ diagram line and its M^1 satellite were performed for zirconium, molybdenum, palladium, and praseodymium. The x-ray spectra were induced by impact with 28-, 40-, 65-, and 100-MeV α particles and measured with a transmission-type bent crystal spectrometer in modified DuMond slit geometry. From the relative yields of the $K\beta_2M^1$ satellites the experimental average M-shell ionization probabilities for nearly central collisions were deduced. They are compared with theoretical predictions from the semiclassical independent particle approximation using either hydrogenlike wave functions (SCA-HWF) or Dirac-Hartree-Fock wave functions (SCA-DHF), pointing out the relevance of the use of DHF wave functions instead of hydrogenlike wave functions in the SCA model. Moreover, the experimental energy shifts of the satellite transitions with respect to the diagram lines are compared to results of extensive multiconfiguration Dirac-Fock calculations. [S1050-2947(98)03801-3]

PACS number(s): 34.50.Fa, 32.30.Rj, 32.70.Jz, 32.80.Fb

I. INTRODUCTION

During the last two decades, inner-shell ionization processes in ion-atom collisions have become a subject of intensive research. The results are used in many disciplines [1], such as, e.g., trace element analysis, ion implantation, astrophysics, solid state physics, atmospheric physics, fusion diagnostic studies, x-ray lasers, and nuclear physics. It is well established that in particle-induced x-ray emission multiply ionized states give rise to so-called satellite transitions that result from the angular momentum coupling of different hole configurations. As a consequence of the change in the electron screening of the nuclear charge, the x-ray satellites are shifted in energy with respect to the diagram lines. Thanks to high-resolution x-ray diffractometry measurements the knowledge about multiply ionized atoms as well as processes by which inner-shell vacancies are produced has been considerably enriched over the last few years.

Probabilities for particle-induced K-shell ionization have already been measured with great accuracy for wide ranges of target elements and projectile energies. Experimental results are well reproduced by first-order perturbation theories. On the contrary, the processes leading to the ionization of higher shells are not yet fully understood and are still subject of investigations, both theoretically and experimentally. Concerning the M-shell ionization induced by light ions, only few experimental data do exist ([2–6] and references therein), giving total M-shell or subshell ionization cross sections for heavy atoms. For target atoms with $Z<60$ the M-shell ionization data are very scarce [6]. Existing results concern mainly Auger electron production cross sections [7] and electron capture cross sections [8]. A few years ago, our group started a study of the multiple inner-shell ionization induced in mid-Z atoms by the impact of energetic ions [9–18]. In particular, a method for the determination of the M-shell ionization probability in central collisions was proposed [11]. Using a high-resolution DuMond-type curved crystal spectrometer [19], it was possible to resolve the M^1 satellite from the parent diagram line $K\beta_2$ ($4p$-$1s$) for several medium-mass atoms. From the measured relative satellite intensities the ionization probabilities were extracted. It is worth noting that in this method, which is described in detail in [12,17], the rather large uncertainties characterizing the available fluorescence and Coster-Kronig yields only moderately influence the determination of the satellite-to-diagram line intensity ratios. We previously used a similar technique to study the L- and M-shell ionization probabilities of several medium-Z targets bombarded by $^4\text{He}^{2+}$ ions [11–13,20]. Systematic deviations between the measured ionization probabilities and the theoretical predictions of the semiclassical approximation (SCA) version of Trautmann and Rösel [21,22] were observed. The discrepancy was found to grow with increasing values of the projectile reduced velocity. In experiments with $^{16}\text{O}^{8+}$ ions the same trend was evinced [10,14,15]. Since the observed discrepancies were attributed mainly to the use of inadequate hydrogenlike wave functions in the SCA calculations, an improved version of the SCA model was developed, in which the single-electron ionization probabilities were calculated with more realistic Dirac-Hartree-Fock electronic wave functions [23,24]. These improved SCA calculations resulted in a much better agreement between experimental and theoretical L- and M-shell ionization probabilities, showing the importance of the choice of proper wave functions in the SCA

calculations for ''fast'' ion-atom collisions.

As the above-mentioned experiments covered only a narrow interval with respect to the projectile reduced velocity, a new series of measurements was undertaken in which several medium-mass elements (Zr, Mo, Pd, and Pr) were bombarded with $^4\mathrm{He}^{2+}$ ions of various energies, ranging from 7 to 25 MeV/nucleon. The L-shell ionization probabilities that were deduced from the relative yields of the $K\alpha_{1,2}L^1$ and $K\beta_{1,3}L^1$ satellites have been presented and discussed in a previous paper [25]. In the present study results concerning the M shell are reported.

For the M shell, the investigated collisions correspond to projectile reduced velocities that range from ~ 1.8 to ~ 7.2. The ionization probabilities were determined from the relative yields of the $K\beta_2M^1$ satellites. The obtained results were compared to theoretical SCA predictions using either hydrogenlike wave functions (SCA-HWF) or Dirac-Hartree-Fock wave functions (SCA-DHF). The energy shifts of the satellites were also determined and compared to results of extensive multiconfiguration Dirac-Fock (MCDF) calculations.

In the case of fast particle impact, the direct Coulomb ionization is accompanied by ionization due to multielectron processes such as shakeoff and shakeup. In addition, for solid targets, the intensity of the $K\beta_4$ ($4d$-$1s$) transition that has approximately the same energy as the $K\beta_2M^1$ satellite is strongly enhanced by solid state effects [26] and may thus contribute significantly to the measured satellite yield. Assuming that shake-up and solid-state effects are independent of the K-shell ionizing process, we have determined their contribution to the satellite intensity by comparing the He^{2+}-induced $K\beta_2$ spectra with the corresponding photoinduced spectra. Furthermore, as the K-absorption edge of the investigated elements lies in the energy region of the $K\beta_2M^1$ satellite, the spectra were corrected for the self-absorption in the targets. Thus the K edges of all elements were precisely measured to allow a proper correction of the particle-induced and photoinduced spectra.

II. EXPERIMENTAL SETUP

The α-particle-induced spectra were measured at the variable energy Philips cyclotron of the Paul Scherrer Institute (PSI) in Villigen, Switzerland. Beam currents of $1–4$ μA were used, depending on the investigated elements. The energies of the delivered α particles were 28, 40, 65, and 100 MeV.

The measurements were performed with an on-line transmission-type curved-crystal spectrometer. A detailed description of the instrument can be found in Ref. [19]. The spectrometer was operated in the modified DuMond-slit geometry, which has the advantage that thermal deformations of the target do not influence the line shapes in the measured spectra.

The targets consisted of 4×40-mm^2 self-supported metallic foils having the following thicknesses: 12.6 mg/cm^2 for $_{40}$Zr, 23.0 mg/cm^2 for $_{42}$Mo, 30.1 mg/cm^2 and 31.7 mg/cm^2 for $_{46}$Pd, and 14.0 mg/cm^2 for $_{59}$Pr. They were mounted on a special aluminum holder and positioned 2 cm behind the slit. Furthermore, they were tilted at 10° with respect to the target-crystal direction. This angle was chosen as a compromise between the self-absorption of the x rays in the target and the size of its area seen by the crystal through the slit.

The x rays were diffracted by the (110) planes of a 10×10-cm^2 SiO$_2$ crystal plate of 2.5-mm thickness, bent cylindrically to a radius of 3.15 m. The effective reflecting area was about 5×5 cm^2. Except for the 100-MeV measurements the reflectivity of the crystal was enhanced by a factor of 2–4 by applying a high-frequency alternating electric field across the lamina. The electric field produces periodic deformations of the reflecting planes, inducing thus a quasimosaicity that increases the reflectivity of the crystal [27].

The diffracted x rays were detected by a 1-mm-thick NaI scintillation detector surrounded by an anti-Compton ring. The beam intensity was monitored, using a semiconductor detector, which was placed in front of the slit, slightly below the target-crystal axis. The monitor-detector viewed the target through the same slit as the crystal, in order to account for possible fluctuations of the beam position on the target. The energy region measured by the monitor detector corresponded to that of the target K x rays.

The photoinduced x-ray spectra were measured at the University of Fribourg, Switzerland, using a similar DuMond-type curved crystal spectrometer (see, e.g., [28,29]). The spectra were induced by means of a commercial 3-kW x-ray tube equipped with a gold anode and a window sheet of nonporous beryllium. The tube was water cooled and operated at 80 kV and 30 mA. It was oriented so that the ionizing radiation was perpendicular to the target-crystal direction. The tube to target distance was 45 mm. The same crystal plate as the one employed at PSI was used. The diffracted x rays were recorded with a 5 in.-diameter and 0.25 in. NaI(Tl)+2 in. CsI(Tl) thick phoswich detector (The Harshaw Chemical Co., Crystal and Electronics Products Dept., OH 94139).

To correct the steplike decrease in the spectra due to the self-absorption in the target, we measured the K absorption edges of the investigated elements. For each target the self-absorption variation as a function of the photon energy was determined. For this purpose the spectrometer was employed as a monochromator, the x-ray tube anode being viewed directly by the crystal through the slit. The absorbers were installed in front of the Soller slit collimator placed between the crystal and the detector. The K-edge measurements were performed two times, once with the alternating electric field applied to the crystal and once without electric field. This was dictated by the fact that the crystal reflectivity enhancement due to the ac field is accompanied in general by some broadening of the instrumental response.

The instrumental response of the spectrometer, which depends mainly on the slit width, the imperfect crystal curvature and the applied ac voltage, was determined by measuring the 25.65150(7)-keV γ decay line of a ^{161}Tb calibration source [30]. The obtained full width at half maximum (FWHM) of the Gaussian function representing the instrumental line shape, was found to be 10.5 ± 0.5 arcsec without, and 12.9 ± 0.9 arcsec with the alternating electric field applied to the crystal.

All spectra were measured in first order of reflection. The angles of the reflected x rays were measured by means of an optical laser interferometer, which is described in detail in [19]. The zero Bragg angle of the spectrometer was deter-
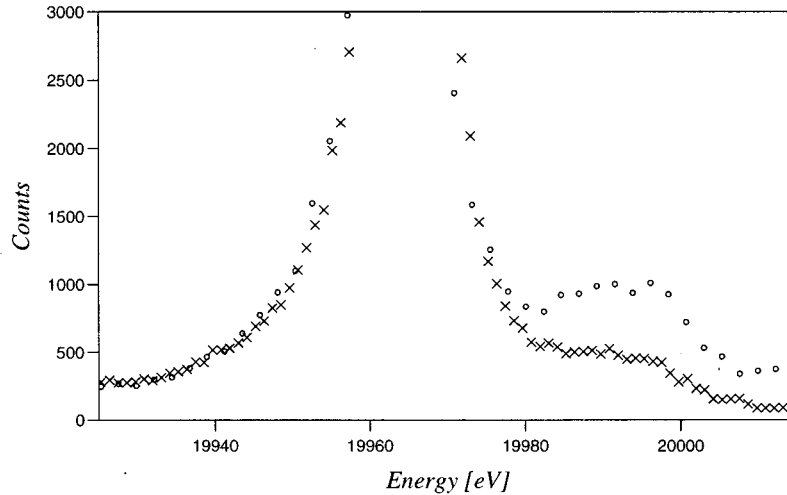
FIG. 1. Comparison of the photoinduced ($\times$) and the 100 MeV α-induced ($\bigcirc$) $K\beta_2$ spectra of molybdenum. One sees that in the α-induced spectrum the M-satellite yield does not only reflect the direct Coulomb ionization but also the M-shake contribution and the $K\beta_4$ transition. Both spectra were normalized to give the same $K\beta_2$ peak heights.

mined by measuring for each target the $K\beta_{1,3}$ line on both sides of reflection whereas the energy calibration was based on the $K\beta_1$ energies quoted by Bearden [31]. For illustration the $K\beta_2$ spectra of molybdenum resulting from photon and 100-MeV He^{2+} ion bombardment are presented in Fig. 1.

III. DATA ANALYSIS

A. Correction for the *K*-absorption edge

As for medium-mass elements the K-absorption edges are lying in the region of the $K\beta_2M^1$ satellite, it is of prime importance to correct the spectra for the self-absorption in the target. This was done for the photoinduced as well as for the α-induced spectra using the K-absorption edge measurements. For the photoinduced spectra, the known spectral intensity distribution of the x-ray tube was used to determine

the variation of the target activity as a function of the penetration depth of the ionizing radiation. On the contrary, the α-induced ionization was assumed to be constant over the entire target thickness. It is reasonable to make this assumption since, due to the small energy loss (order of a few percent) of the α particles in the targets, the K-shell ionization cross sections can be considered as nearly constant throughout the target thickness. The measured K-absorption edge of Zr as well as the raw and corrected $K\beta_2$ spectra of the same element are shown for illustration in Fig. 2.

B. Fitting procedure

As the M-shell spectator vacancy can be located in different subshells and because there are many possibilities to couple this vacancy with the $1s$ hole in the initial state and the $4p$ hole in the final state, $K\beta_2M^1$ satellites consist of
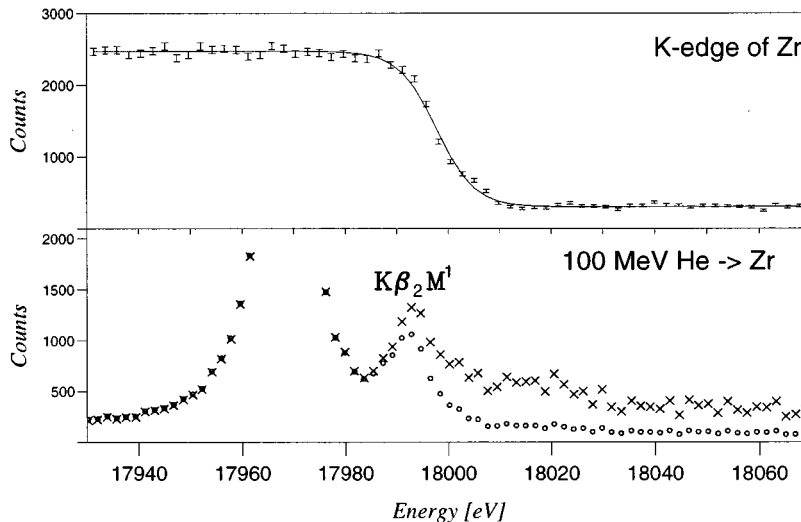

FIG. 2. The upper part shows the K edge of Zr. In the lower part, showing the $K\beta_2$ diagram line and $K\beta_2M^1$ satellite, a comparison of the measured ($\bigcirc$) and the K-edge corrected ($\times$) spectra of zirconium is presented. It is obvious that the background fluctuations above the K edge are increased due to this correction.
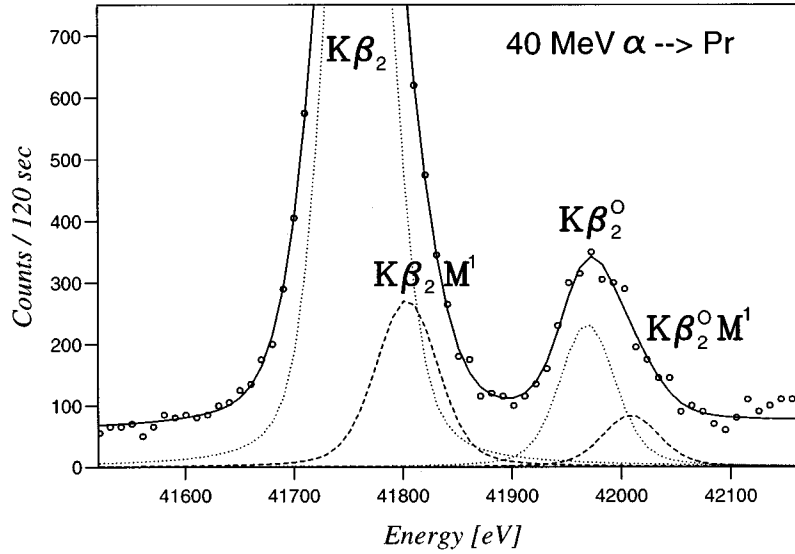
FIG. 3. Enlarged crystal spectrometer spectrum of praseodymium induced by 40-MeV ^{4}He^{2+} ions. The dotted lines represent the fitted diagram transitions $K\beta_2$ and $K\beta_2^O$ ($5p$-$1s$), the dashed ones the M^1 satellites of these two lines, whereas the solid line stands for the total fit, i.e., the sum of the components added to the background.

numerous components that have different transition probabilities and slightly different energies distributed about an average value. For this reason the data analysis was performed with the method described by Carlen *et al.* [14,15]. In this method, which was developed to analyze K x-ray spectra of multiply ionized atoms, a particular x-ray line is assumed to be a linear combination of all components contributing to the transition. The theoretical energies and transition probabilities of the individual components are determined by means of extensive MCDF calculations. The final result of the MCDF calculations is a ''stick'' spectrum consisting of many linebars. To compare with the experiment the linebars are given a Voigtian profile, which results from the convolution of the Gaussian instrumental broadening with the Lorentzian function representing the natural line shape of the components. The transition line shape is then constructed by computing the weighted sum of the Voigt functions corresponding to the different components, the weighting factors being given by the transition probabilities of the latter. In the present study the MCDF calculations were performed with the MSAL (modified special average level) version [17,32,33] of the code GRASP [34], which allows relativistic calculations including the transverse Breit interaction and QED corrections (self-energy and vacuum polarization).

For Pd for which all subshells are closed in the ground state, the $K\beta_2 M^1$ satellite consists of 72 components. If more than one subshell is open in the ground state as is the case for the other investigated targets, the number of components increases so drastically that the method is no longer tractable. For this reason we have adopted for the MCDF calculations of Zr, Mo, and Pr the modified ground-state configurations [Kr]$4d^05s^2$ [Kr]$4d^4_{3/2}4d^0_{5/2}5s^2$ and [Xe]$4f^06s^2$, respectively, which are characterized by either full or empty subshells. Comparing the MCDF results obtained from these simplified configurations with the ones obtained from the real configurations [Kr]$4d^25s^2$ (Zr), [Kr]$4d^55s^1$ (Mo) and

[Xe]$4f^36s^2$ (Pr), only small energy shifts and insignificant changes in the line shapes were found for the $K\beta_2$ diagram lines.

The observed $K\beta_2$ spectra, corrected for the self-absorption in the targets, were thus analyzed with a least-squares-fitting computer program (package MINUIT [35], CERN library), employing theoretical shapes determined by the above-mentioned MCDF calculations to reproduce the profiles of the diagram and satellite lines. The relative intensities and average energy shifts of the satellite groups with respect to the parent diagram lines were let free in the fit. For a particular target element, the same Voigt profile was given to all MCDF components, keeping fixed the instrumental broadening at its known value but letting free the natural linewidth in order to account for the unresolved N-shell satellites. A constant background was further used as a free fitting parameter. The fitted $K\beta_2$ spectrum of Pr is shown for illustration in Fig. 3. One can notice that for this element the MCDF method of analysis was particularly useful since the M^1 satellites of the $4p$-$1s$ and $5p$-$1s$ transitions are not resolved from the parent diagram lines but just appear as weak asymmetries on the high-energy flank of the latter. In Fig. 4 the fit of the Zr $K\beta_2$ spectrum is depicted together with the MCDF ''stick'' spectra corresponding to the diagram line and the first-order and second-order M satellites. Except for Pr, second-order M satellites could be indeed observed in spite of their very weak intensities. They were included in the fitting procedure because, as shown in Fig. 4, they may contribute somewhat to the observed yields of the M^1 satellites with which they partly overlap. The dependence of the M-satellite intensity on the α-particle energy is illustrated in Fig. 5. The same figure shows also the influence of the M^2 satellite, whose relative intensity varies with the beam energy.

C. Electron rearrangement

The satellite yields extracted from the fitting procedure reflect the hole distribution in the atom at the moment of the
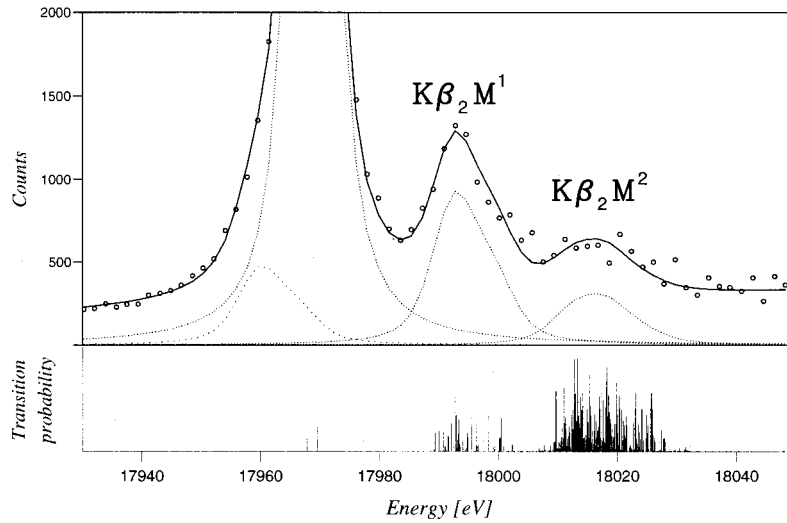
FIG. 4. $K\beta_2$ crystal spectrometer spectrum of zirconium induced by 100-MeV ^{4}He^{2+} ions, showing the diagram line $K\beta_2$ as well as the satellites M^1 and M^2. The dotted line on the low-energy side of the diagram line represents the asymmetry observed in some of the measured spectra. The stick spectrum in the lower part of the figure represents the MCDF predictions.

K x-ray emission and not the initial hole distribution induced by the collision. Therefore, the fitted relative intensities of the M satellites were corrected for those electron rearrangement processes that modify the number of M-shell vacancies and take place prior to the K x-ray emission. These processes were accounted for by a statistical scaling procedure [10,36]. Changes of the M-satellite yields are due mainly to the M Auger effect, which transfers the M vacancies to higher shells, whereas M radiative transitions have very weak strengths and can be neglected. L holes can be moved to the M shell through LMN Auger and LLM Coster-Kronig transitions. However, since in the collisions investigated in the present study the creation of KL double-vacancy states is about one order of magnitude smaller than the excitation of KM states, these processes were not considered in the rearrangement calculations. The same holds for the M-shell super-Coster-Kronig transitions which, depending on the target element, are either forbidden or very weak. The fitted x-ray yields X^n ($n=0,1$) of the $K\beta_2 M^n$ transitions are then related to the initial vacancy yields I^n by the following equations:

$$X^0 = (I^0 + RI^1)\omega_{\beta_2}^0, \tag{1a}$$

$$X^1 = (I^1 - RI^1)\omega_{\beta_2}^1, \tag{1b}$$

where R is a scaling factor describing the electron rearrangement and $\omega_{\beta_2}^n$ represents the partial fluorescence yield of the $K\beta_2$ transition with n spectator holes in the M shell. The
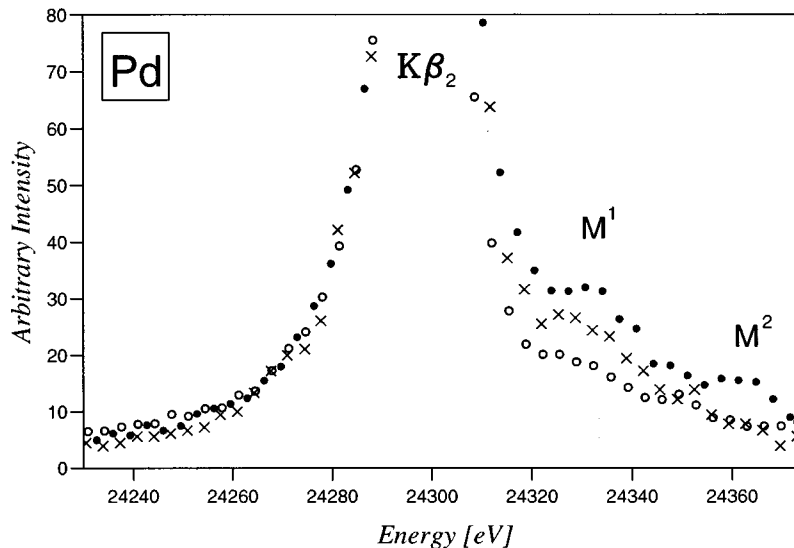

FIG. 5. Comparison of the $K\beta_2$ M-satellite spectra of $_{46}$Pd induced by 40-MeV ($\bullet$), 65-MeV ($\times$), and 100-MeV ($\circ$) α particles. In the 40- MeV α-induced spectra even the M^2 satellite can be observed. All spectra were normalized to give the same $K\beta_2$ peak intensities.

factor R can be written as the weighted sum of the partial rearrangement coefficients R_i, where $i = 1,2,3,4,5$ stands for the different M subshells:

$$R = \sum_i w_i R_i . \qquad (2)$$

Considering the number of electrons in the subshell M_i and assuming identical ionization probabilities per electron for the different subshells, one finds for the weighting factors the following values: $w_1 : w_2 : w_3 : w_4 : w_5 = \frac{1}{9} : \frac{1}{9} : \frac{2}{9} : \frac{2}{9} : \frac{3}{9}$. As only those rearrangement processes that occur prior to the K x-ray emission have to be taken into account one can write for R_i:

$$R_i = \frac{\Gamma_{M_i} - \Sigma_{i<j} \Gamma_{M_i M_j X}}{\Gamma_K + \Gamma_{M_i}} = \frac{\Gamma_{M_i}(1 - \Sigma_{i<j} f_{i,j})}{\Gamma_K + \Gamma_{M_i}}, \qquad (3)$$

where Γ_K and Γ_{M_i} stand for the total widths of the K and the M_i levels and $f_{i,j}$ for the relative Coster-Kronig yields. Using the K and M_i level widths quoted by Krause and Oliver [37] and Campbell and Papp [38], respectively, and the Coster-Kronig coefficients calculated by McGuire [39,40], the following values were obtained for the total rearrangement factors R: 0.033 (Zr), 0.042 (Mo), 0.051 (Pd), and 0.044 (Pr).

Assuming furthermore that the fluorescence yields of the $K\beta_2$ transitions are only weakly affected by the spectator holes in the M shell (i.e., $\omega_{\beta_2}^1 \approx \omega_{\beta_2}^0$), one obtains from Eq. (1) the following ratio for the primary vacancy yields:

$$I_M = \frac{I^1}{I^0} = \frac{X^1/X^0}{1 - R(1 + X^1/X^0)} . \qquad (4)$$

D. Ionization probabilities

To determine the M-shell ionization probability we used the independent-particle approximation. In this framework, the probability that a collision corresponding to an impact parameter b produces m K-shell vacancies and n M-shell holes is given by the expression

$$P_{mK,nM}(b) = \binom{2}{m}\binom{18}{n}[p_K(b)]^m[1 - p_K(b)]^{2-m}$$
$$\times [p_M(b)]^n[1 - p_M(b)]^{18-n}, \qquad (5)$$

where p_K represents the K-shell ionization probability per electron and p_M the mean value of the M-subshell ionization probabilities per electron. Integration of this expression over the impact parameter b delivers then the corresponding cross sections. As for charged particle impact p_M is essentially constant in the impact parameter range $(0, b_{\max})$, where the K-shell ionization occurs, one finds

$$\frac{\sigma_{1K,1M}}{\sigma_{1K,0M}} = I_M = \frac{18 p_M}{1 - p_M}, \qquad (6)$$

where I_M is the primary vacancy yield ratio defined in (4). Using the relations (4) and (6), one obtains finally

$$p_M = \frac{X^1/X^0}{X^1/X^0 + 18[1 - R(1 + X^1/X^0)]} . \qquad (7)$$

IV. RESULTS AND DISCUSSION

A. M-shell ionization accompanying α-particle impact

Competitive processes

The main process responsible for the production of the multiple ionization is the direct Coulomb interaction between the charged particle and the bound electrons of the target atom. Other processes of less importance may, however, contribute to the creation of inner-shell vacancies. Among these competitive processes, the most important are the electron capture, the target activation, and the electron coupling effects.

The electron capture is the transfer of bound target electrons to the projectile. In our case, the only case to consider is the capture of an M-shell target electron to the K shell of the fully stripped He ions. Using the theory presented in [41–43], the contribution of this process can be estimated. The total cross section for the direct Coulomb ionization of an M-shell electron is some Mbarn (calculated with the SCA theory), whereas the cross section for the capture of an electron from the M shell of the target atom to the K shell of the projectile is in the order of kbarn. Assuming a similar impact-parameter dependence as for the direct ionization, we can certainly neglect the electron capture probability with respect to the direct ionization probability, even if the above assumption is only strictly valid in the slow collision limit [41].

The target activation, due to (α, xn) reactions and Coulomb nuclear excitation may also produce additional K-shell holes. This K-shell ionization can be produced via photoionization by γ rays emitted by the final nucleus or by the K-shell internal conversion process. However, as for the investigated collisions the cross sections of the above-mentioned nuclear reactions are several orders of magnitude smaller than the cross sections for the atomic direct Coulomb excitation, the influence of the target activation on the primary vacancy distribution is completely negligible.

In most approximations the ionization probabilities or cross sections are calculated using the independent particle model, which postulates that each electron moves independently in a mean potential made up of the nuclear charge minus the shielding of other electrons. This potential, however, contains only a part of the mutual electron-electron interaction. Deviations of the independent particle model may be understood as electron correlation [44–46]. The most important correlation effect is the shake process. In this process, due to the sudden change of the atomic potential following the creation of a core vacancy, electrons can be excited to higher unfilled bound states (shakeup) or to continuum states (shakeoff) [47–49]. For a given core vacancy, the shake probability grows with the principal quantum number of the shaken electron and its dependency on the atomic number is approximately Z^{-2}. As the direct Coulomb ionization is proportional to the squared charge of the projectile, in collisions involving mid-Z elements and light charged particles, a significant part of the observed KM double ionization may thus result from electron shake pro-

TABLE I. Experimental M-satellite yields relative to $K\beta_2$ for photoionization as well as for the α-particle induced spectra.

Element	Photoionization	28 MeV α	40 MeV α	65 MeV α	100 MeV α
$_{40}$Zr	8.39 ± 0.35[a]	27.6 ± 1.2	21.3 ± 1.3	13.8 ± 0.8	16.9 ± 1.6
$_{42}$Mo	8.60 ± 0.36[a]				13.6 ± 0.7
$_{46}$Pd	2.46 ± 0.24[a]		14.9 ± 0.8	11.7 ± 0.9	6.1 ± 0.4
$_{59}$Pr	1.55 ± 0.60	9.9 ± 1.3	11.7 ± 1.4	6.7 ± 0.9	6.2 ± 0.6

[a]Measured with the same instrument and already published [17].

cesses in the M shell following the $1s$ vacancy production. Furthermore, the quadrupole-allowed $K\beta_4$ ($4d$-$1s$) transition is also expected to contribute to the observed M^1 satellite yields. It was possible to take care of the M^1 satellites intensity surplus due to the shake effects and $K\beta_4$, by subtracting from the relative particle-induced satellite yields those obtained in the photoionization measurements. More concretely, the x-ray yield ratios X^1:X^0 used in Eq. (7) were determined as follows:

$$\frac{X^1}{X^0} = \left(\frac{I(K\beta_2 M^1)}{I(K\beta_2 M^0)}\right)_\alpha - \left(\frac{I(K\beta_2 M^1)}{I(K\beta_2 M^0)}\right)_{photo}. \qquad (8)$$

A comparison between the α-particle-induced and photo-induced $K\beta_2$ spectra of Mo is presented in Fig. 1, whereas the fitted $I(K\beta_2 M^1)$:$I(K\beta_2 M^0)$ yield ratios corresponding to both excitations are listed for all target elements in Table I. Quoted uncertainties are purely statistical and do not include systematic errors as those arising for instance from the MCDF determined line shape of the transitions or from the corrections for the self-absorption in the target.

Ionization probability p_M

The average M-shell ionization probabilities per electron p_M were determined from the relation (7). Results are given in Table II. Indicated errors originate mainly from the uncer-

tainties on the particle-induced and photoinduced x-ray yields. For the rearrangement factors an uncertainty of $\sim 20\%$ was included in the calculation of the errors. The quoted effective beam energies were calculated by taking into account the stopping power of the target, the energy dependence of the K-shell ionization cross sections, and the self-absorption of the x rays in the target. As the shake and $K\beta_4$ transition contributions to the satellite yields were subtracted beforehand and are thus not included in the x-ray yield ratios X^1:X^0 of Eq. (7), the values p_M quoted in Table II correspond to the direct Coulomb excitation process only. Furthermore, since in the experimental method employed in our study we have considered only the M-shell ionization accompanied by a simultaneous K-shell ionization and because the latter decreases very rapidly with the impact parameter, the collisions for which the ionization probabilities were determined may be regarded as nearly central in the M-shell scale.

We have compared our experimental results to theoretical predictions based on the semiclassical approximation (SCA). The advantage of the independent particle SCA model resides in the fact that it allows a detailed comparison with impact-parameter-dependent ionization probabilities. This model was introduced and developed originally by Bang, Hansteen, and co-workers [50]. Most of the SCA formulations are derived from the first-order perturbation theory, re-

TABLE II. Comparison of the corrected experimental ionization probabilities p_M with theoretical predictions. The reduced velocity was calculated using Eq. (9).

Target	Effective beam energy E_P	Reduced velocity η	Average M-shell ionization probabilities		
			Expt.	SCA-HWF	SCA-DHF
$_{40}$Zr	26.7 MeV	3.73	0.0110(7)	0.00350	0.01216
	39.0 MeV	4.51	0.0074(8)	0.00239	0.00838
	64.3 MeV	5.80	0.0031(5)	0.00144	0.00507
	99.5 MeV	7.21	0.0049(9)	0.00092	0.00325
$_{42}$Mo	26.8 MeV	3.41	0.0177(9)[a]	0.00353	0.01199
	99.3 MeV	6.57	0.0029(4)	0.00094	0.00324
$_{46}$Pd	26.8 MeV	2.88	0.014(2)[a]	0.00357	0.01194
	38.5 MeV	3.46	0.0073(5)	0.00250	0.00849
	63.9 MeV	4.45	0.0054(5)	0.00150	0.00516
	99.2 MeV	5.55	0.0021(3)	0.00096	0.00331
$_{59}$Pr	26.6 MeV	1.81	0.0048(8)	0.00371	0.00940
	38.9 MeV	2.18	0.0059(8)	0.00262	0.00692
	64.2 MeV	2.81	0.0030(6)	0.00163	0.00441
	98.8 MeV	3.49	0.0027(5)	0.00106	0.00292

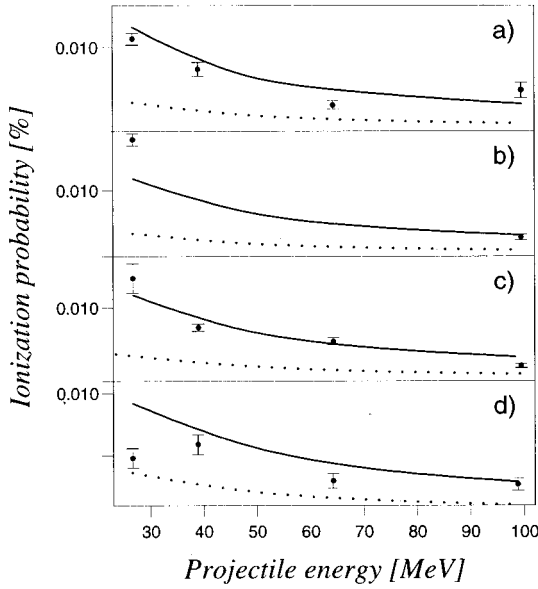[a]Taken from an earlier publication [12] for comparison.

FIG. 6. *M*-shell ionization probability per electron as a function of the $^4\mathrm{He}^{2+}$ projectile energy for (a) $_{40}$Zr, (b) $_{42}$Mo, (c) $_{46}$Pd, and (d) $_{59}$Pr. The solid line shows an interpolation of the calculated SCA-DHF ionization probabilities, whereas the dotted line represents an interpolation of the SCA-HWF calculations. Our experimental results are indicated by the full circles.
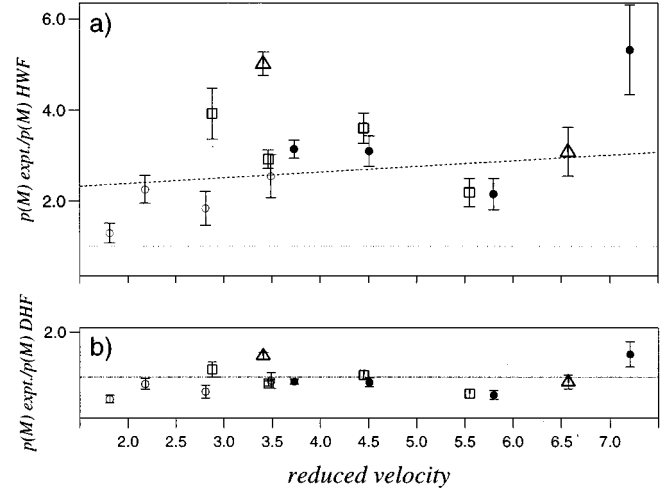

FIG. 7. Ratio of the experimental average *M*-shell ionization probability per electron and the theoretical predictions vs the reduced velocity η for the investigated targets zirconium (●), molybdenum (△), palladium (□) and praseodymium (○). In (a) the experimental results are compared to SCA predictions using hydrogenlike wave functions, whereas in (b) Dirac-Hartree-Fock (DHF) were used. The same vertical axis scale is used for both parts to allow a better comparison of the two models. The dotted lines correspond to a ratio of 1. In (a) the dashed line corresponds to the weighted least-squares fit of the data to a straight line.

quiring that the target atomic number is much higher than that of the projectile. The present calculations were performed by means of the modified SCA version of Trautmann and Rösel [21,22], using either relativistic hydrogenlike wave functions (SCA-HWF) or Dirac-Hartree-Fock (SCA-DHF) wave functions. The Dirac-Hartree-Fock wave functions for the bound electrons of the target-atom were calculated with the GRASP program, whereas the continuum states were computed using the adapted code for GRASP, CONTWVG [23,24]. As the coupled-channel effects were not included in our calculations, a statistical average over all subshells pertaining to the same shell was taken. For all elements and beam energies the HWF as well as the DHF calculations were performed with an impact parameter of $b_K^{\mathrm{eff}}=500$ fm. In both calculations hyperbolic projectile paths and recoil effect of the target nucleus were included. Experimental values of the binding energies in the separated atom mode were used. In all considered cases five multipole moments proved to be accurate enough. The obtained results are listed in Table II.

The experimental ionization probabilities are plotted in Figs. 6(a)–6(d), where they are compared to the SCA-HWF and SCA-DHF theoretical predictions. In Fig. 7, the ratios of the experimental to theoretical *M*-shell ionization probabilities ($p_M^{\mathrm{expt.}}/p_M^{\mathrm{theo.}}$) are plotted as a function of the reduced projectile velocity. The reduced velocity η was calculated using the following formula:

$$\eta=\frac{v_{\mathrm{projectile}}}{v_{\mathrm{electron}}}=\sqrt{\frac{E_p m_e}{E_{\mathrm{bind}} M_P}}, \qquad (9)$$

where m_e and M_P are the electron and projectile masses, respectively, E_{bind} the average *M*-shell electron binding en-

ergy, and E_p the kinetic energy of the projectile. The average binding energy of the *M*-shell electrons was found to be $E_{\mathrm{bind}}=264$ eV for Zr, $E_{\mathrm{bind}}=315$ eV for Mo, $E_{\mathrm{bind}}=442$ eV for Pd, and $E_{\mathrm{bind}}=1114$ eV for Pr.

It can be seen that calculations using hydrogenlike wave functions underestimate the experimental *M*-shell ionization probability for all measured targets and all He^{2+}-beam energies by a factor of about 2–5. The same trend was observed for the *L*-shell ionization probability at somewhat smaller reduced velocities ($0.8 \leqslant \eta \leqslant 2.4$) [25]. In that previous work, except for reduced velocities smaller than 1 (i.e., $v_{\mathrm{projectile}} < v_{\mathrm{electron}}$), the SCA calculations using hydrogenlike wave functions were found to underestimate the experimental ionization probability, as in the present study, but the discrepancies between the experimental values and the SCA-HWF calculations were smaller. It was further found that the discrepancy increases with growing values of the projectile reduced velocity. This observation is more or less confirmed by the present *M*-shell ionization study [see Fig. 7(a)].

On the other hand, it can be seen that the experimental ionization probabilities are in quite good agreement with the SCA-DHF predictions over the whole range of the reduced projectile velocity covered by our experiment. The experimental to theoretical ionization probability ratios are almost uniformly scattered around 1, confirming thus the observation already made in the mentioned *L*-shell ionization study [25] that much better agreements between theory and experiment are obtained when DHF wave functions are used in the SCA model instead of DHF wave functions.

In some of the particle-induced spectra, the $K\beta_2 M^2$ satellite could also be observed. However, as the fitted intensity was extremely small and in most cases even smaller than the

TABLE III. Energy of the $K\beta_2$ diagram line in comparison with the MCDF calculations and standard values [57]. In the right columns, the experimental and the computed (MCDF) energy shifts $K\beta_2 M^1 - K\beta_2 M^0$ are listed. All energies are given in eV.

| Element | Projectile energy (MeV) | Energy of $K\beta_2$ transition | | | E($K\beta_2 M^1$) − E($K\beta_2 M^0$) | |
		Expt.	MCDF	Ref. [57]	Expt.	MCDF
$_{40}$Zr	26.7	17968.6(6)	17974.0	17969	24.0(1.6)	27.1
	39.0	17968.5(6)	17974.0	17969	22.9(1.7)	27.1
	64.3	17967.9(7)	17974.0	17969	24.0(1.9)	27.1
	99.5	17968.8(6)	17974.0	17969	25.8(1.7)	27.1
$_{42}$Mo	99.3	19961.1(7)	19964.5	19965	28.6(1.3)	29.7
$_{46}$Pd	38.5	24299.5(7)	24296.4	24298	29.2(1.0)	30.9
	63.9	24299.5(7)	24296.4	24298	29.0(1.3)	30.9
	99.2	24298.2(8)	24296.4	24298	28.4(1.4)	30.9
$_{59}$Pr	26.6	41764.3(6)	41764.0	41768	50.4(1.4)	50.5
	38.9	41763.8(5)	41764.0	41768	48.5(1.2)	50.5
	64.2	41767.4(5)	41764.0	41768	41.5(1.4)	50.5
	98.8	41764.4(6)	41764.0	41768	46.0(1.5)	50.5

corresponding error, the M^2 satellites were not considered for the determination of the ionization probabilities p_M.

Energies

As already mentioned in the Introduction, satellites are shifted with respect to the parent diagram lines towards higher energies, due to the change of the screening caused by the presence of the spectator vacancy. The energy shift depends on the electron configuration describing the initial state of the ionized target atom. In the present study the initial state is characterized by one K-shell hole, zero or one M-shell hole and an unknown number of outer-shell vacancies. As the energy shift due to the presence of outer shell holes is small compared to the natural linewidths of the diagram and satellite transitions, the outer-shell ionization does not give rise to additional, resolved $K\beta_2$ satellites, but broadens the observed lines and may produce a visible asymmetry on their high energy flank. Using MCDF calculations, we have computed the energy shift of the $K\beta_2$ line due to the presence of additional N-shell vacancies. The calculated shifts range from 0.9 to 5.5 eV for Mo and from 5.3 to 11.0 eV for Pr. As the shifts of the $K\beta_2$ centroids depend on the intensity of the unresolved N satellites, a variation with the projectile energy is expected. However, as both $K\beta_2 M^0$ and $K\beta_2 M^1$ centroids are shifted almost equally, one additional N hole has practically no influence on the energy separation between these two lines. This is confirmed by the Table III, where the energy difference between the $K\beta_2$ diagram line and the M^1 satellite is practically constant, except for Pr. The quoted experimental energy shifts are in good agreement with the MCDF calculations for the elements Mo and Pd. For Zr and Pr, they are slightly smaller than the calculated ones.

On the other hand, the shift of the $K\beta_2$ centroids as a function of the projectile energy does not seem to be significant, at least for the elements Zr and Pd for which the variation of the energy shift is smaller than the corresponding uncertainties. For Pr there is some trend of the energy shift to decrease with the beam energy. However, no definitive conclusion could be drawn from this observation, which is per-

haps related to the poor separation between the $K\beta_2 M^0$ and $K\beta_2 M^1$ lines in the case of Pr. Energy shifts induced by additional O-shell vacancies are about ten times smaller and were thus neglected.

B. *M*-shell ionization accompanying *K*-shell photoionization

Importance of the $K\beta_4$ transition

In the photoinduced $K\beta_2$ spectra of Zr, Mo, and in a smaller extent Pd, the x-ray yields observed in the energy region of the M^1 satellites cannot be explained by shake processes only. Theoretical calculations based on the sudden approximation (SA) model predict indeed M-shell shake probabilities that are significantly smaller (about three times for Mo) than the values extracted from our photoionization measurements. The reliability of the SA model has been confirmed by a number of experiments and its predictions should thus reproduce our values within a precision of about 20% or better. Furthermore, since for medium-mass elements M-shell electrons are core electrons, it is highly improbable that the discrepancy between the SA predictions and our experimental results resides in the fact that the Zr, Mo, or Pd atom is embedded in a solid. On the other hand, the $K\beta_4$ ($4d$-$1s$) quadrupole-allowed transition lies for all these elements very close in energy to the $K\beta_2 M^1$ satellite. MCDF calculations yield for the energy difference between the $K\beta_4$ and $K\beta_2 M^1$ lines values of only 1.6 eV for Zr, 6.5 eV for Mo, and 5.5 eV for Pd. Therefore the three $K\beta_4$ transitions match, within the experimental resolution, the energies of the M^1 satellites. Free-atom transition probabilities of the $K\beta_4$ line relative to $K\beta_2$ are predicted to be only 3.6×10^{-4} for Zr, 1.1×10^{-3} for Mo, and 3.2×10^{-3} for Pd [51]. However, it was shown recently [17,26,52] that in several $4d$ transition elements the $K\beta_4$ transitions strength is up to 50 times bigger than predicted by free-atom calculations and contributes thus significantly to the surplus of intensity measured in the $K\beta_2 M^1$ satellite region. The strong enhancement of the transition probability was interpreted as being due to the mixing of the $4d$ valence states with p character orbitals. It was

concluded that as a consequence of this orbital overlap a relaxation of the $E2$ selection rules is possible. It has further to be mentioned that a similar intensity enhancement was observed previously for the quadrupole $K\beta_5$ ($3d$-$1s$) transition in the $3d$ transition elements [53,54].

Low-energy tail asymmetry

A slight asymmetry on the low-energy side of the $K\beta_2$ transition was observed in some of the measured spectra. The origin of this asymmetry is not completely clear, but the latter could partially arise from the radiative Auger effect (RAE), a process in which the transition energy is shared between the emitted x ray and a simultaneously ejected bound electron [55]. It has been shown recently that the theoretical predictions of $K-MM$ RAE intensities of Scofield [56] are in quite good agreement with experimental values [29], at least for elements in the range $42 \leq Z \leq 50$. From [56] $I(K-NN(\text{RAE})){:}I(K\beta_2)$ yield ratios varying from $\sim 4.1\%$ (Zr) down to $\sim 2.4\%$ (Pr) are expected. The observed $K\beta_2$ asymmetries were accounted for by using an additional Voigtian in the fit of the $K\beta_2$ line. Depending on the target element, relative intensities varying between 7.1% (Zr) and 2% (Pr) were found for this additional component. It is thus quite probable that a part of the observed asymmetries is due to radiative Auger transitions of the $K-NN$ type. However, as the observed transition lines are broadened due to the presence of additional outer shell holes, no final conclusion can be drawn concerning this problem.

V. CONCLUSION

The $K\beta_2$ x-ray emission of metallic targets of zirconium, molybdenum, palladium, and praseodymium bombarded by 28–100-MeV $^4\text{He}^{2+}$ ions was measured with a high-resolution curved-crystal spectrometer operated in the modified DuMond slit geometry. The $K\beta_2 M^1$ x-ray satellites resulting from the radiative decay of the KM double-vacancy states produced by the collisions could be observed and resolved. The contribution to the observed satellite yields of M-shell electron shake following the $1s$ ionization and of the quadrupole $K\beta_4$ transition, whose intensity is strongly enhanced in $4d$ transition elements, was determined from complementary photoionization measurements. As for medium-mass elements the $K\beta_2 M^1$ satellites lie close to the K edges; the particle-induced and photoinduced spectra were corrected for the self-absorption of the observed x rays in the targets. The KM double ionization due to the direct Coulomb interaction between the charged particles and bound electrons of the target atoms was then determined from the difference between the particle-induced and photoinduced x-ray yields observed in the satellite regions. The so-obtained net satellite yields were further corrected to account for the electron rearrangement processes, which modify the number of M holes and take place before the K x-ray emission. Assuming finally that the K and M electrons are ionized in an uncorrelated way and that the investigated collisions can be considered as nearly central in the M-shell scale, we were able to deduce the M-shell ionization probabilities corresponding to the direct Coulomb excitation only. The projectile reduced velocity interval covered by our study ranges from about 1.8 to about 7.2.

A good agreement with MCDF calculations was found concerning the energy shifts of the M^1 satellites with respect to the parent $K\beta_2$ diagram lines. Regarding the ionization probabilities, we have compared our experimental results with theoretical values obtained from the SCA model. This study has proved that SCA predictions concerning M-shell ionization probabilities of medium-mass elements are improved in a drastic way when relativistic Hartree-Fock wave functions are used for the bound and continuum electrons instead of relativistic hydrogenlike ones. If relativistic hydrogenlike wave functions are employed, the SCA results underestimate the experimental values, discrepancies up to a factor 5 being observed. If, on the contrary, more realistic Dirac-Hartree-Fock wave functions are used, a satisfactory to good agreement is obtained. In a previous work, in which the same collisions were investigated, a similar observation was done for the L-shell ionization [25]. The present study shows that the dependence of the SCA predictions on the choice of the proper wave functions is still more pronounced for the M shell.

---

[1] S. Datz, *The Physics of Electronic and Atomic Collisions*, edited by A. Dalgarno, R. S. Freund, P. M. Koch, M. S. Lubell, and T. B. Lucatorto, AIP Conf. Proc. No. 205 (American Institute of Physics, New York, 1990).

[2] M. Pajek, A. P. Kobzev, and G. Lapicki, Nucl. Instrum. Methods Phys. Res. B **48**, 87 (1990).

[3] A. Bieńkowski *et al.*, Nucl. Instrum. Methods Phys. Res. B **49**, 19 (1990).

[4] M. Pajek *et al.*, Phys. Rev. A **42**, 261 (1990).

[5] A. P. Jesus and J. P. Ribeiro, Nucl. Instrum. Methods Phys. Res. A **280**, 370 (1989).

[6] G. Lapicki, J. Phys. B **23**, 3123 (1990).

[7] H. Kojima *et al.*, J. Phys. Soc. Jpn. **46**, 198 (1979).

[8] S. Andriamonje *et al.*, J. Phys. B **46**, 349 (1985).

[9] B. Perny *et al.*, Z. Phys. D **14**, 37 (1989).

[10] P. Rymuza *et al.*, Z. Phys. D **14**, 37 (1989).

[11] M. W. Carlen *et al.*, Europhys. Lett. **13**, 231 (1990).

[12] M. W. Carlen *et al.*, Z. Phys. D **23**, 71 (1992).

[13] P. Rymuza *et al.*, Z. Phys. D **23**, 81 (1992).

[14] M. W. Carlen *et al.*, Phys. Rev. A **46**, 3893 (1992).

[15] M. W. Carlen *et al.*, Phys. Rev. A **49**, 2524 (1994).

[16] T. Ludziejewski *et al.*, Acta Phys. Pol. B **25**, 699 (1994).

[17] T. Ludziejewski *et al.*, Phys. Rev. A **52**, 2791 (1995).

[18] B. Boschung *et al.*, Phys. Rev. A **52**, 3889 (1995).

[19] B. Perny *et al.*, Nucl. Instrum. Methods Phys. Res. A **267**, 120 (1988).

[20] B. Perny *et al.*, Phys. Rev. A **36**, 2120 (1987).

[21] D. Trautmann and F. Rösel, Nucl. Instrum. Methods **169**, 259 (1980).

[22] D. Trautmann, F. Rösel, and G. Baur, Nucl. Instrum. Methods Phys. Res. **214**, 21 (1983).

[23] W. F. Perger, Z. Halabuka, and D. Trautmann, Comput. Phys. Commun. **76**, 250 (1993).

[24] Z. Halabuka, W. Perger, and D. Trautmann, Z. Phys. D **29**, 151 (1994).

[25] B. Boschung *et al.*, Phys. Rev. A **51**, 3650 (1995).

[26] J. Hoszowska and J.-Cl. Dousse, J. Phys. B **29**, 1641 (1996).

[27] J.-Cl. Dousse and J. Kern, Acta Crystallogr., Sect. A: Cryst. Phys., Diffr., Theor. Gen. Crystallogr. **36**, 966 (1980).

[28] J. Hoszowska, J.-Cl. Dousse, and Ch. Rhême, Phys. Rev. A **50**, 123 (1994).

[29] Ch. Herren and J.-Cl. Dousse, Phys. Rev. A **53**, 717 (1996).

[30] B. Jeckelmann *et al.*, Nucl. Instrum. Methods Phys. Res. A **241**, 191 (1985).

[31] J. A. Bearden and A. F. Burr, Rev. Mod. Phys. **39**, 78 (1967).

[32] K. G. Dyall *et al.*, Comput. Phys. Commun. **55**, 425 (1989).

[33] M. Polasik, Phys. Rev. A **40**, 4361 (1989).

[34] L. P. Grant *et al.*, Comput. Phys. Commun. **21**, 207 (1980).

[35] F. James and M. Roos, Comput. Phys. Commun. **10**, 343 (1975).

[36] M. Pajek *et al.*, Nucl. Instrum. Methods Phys. Res. B **52**, 109 (1990).

[37] M. O. Krause and J. H. Olivier, J. Phys. Chem. Ref. Data **8**, 329 (1979).

[38] J. L. Campbell and T. Papp, X-Ray Spectrom. **24**, 307 (1995), and references therein.

[39] E. J. McGuire, Phys. Rev. A **5**, 1043 (1972).

[40] E. J. McGuire, Phys. Rev. A **5**, 1052 (1972).

[41] G. Lapicki and W. Losonsky, Phys. Rev. A **15**, 896 (1977).

[42] G. Lapicki and F. D. MacDaniel, Phys. Rev. A **22**, 1896 (1980).

[43] V. S. Nikolaev, Zh. Eksp. Teor. Fiz. **51**, 1263 (1966) [Sov. Phys. JETP **24**, 847 (1967)].

[44] J. H. McGuire, Phys. Rev. A **36**, 1114 (1987).

[45] N. Stolterfoht, Phys. Scr. **42**, 192 (1990).

[46] J. F. Reading and A. L. Ford, Comments At. Mol. Phys. **23**, 301 (1990).

[47] T. A. Carlson and M. O. Krause, Phys. Rev. **140**, 1057 (1965).

[48] T. Åberg, Phys. Rev. **156**, 35 (1967).

[49] M. O. Krause, T. A. Carlson, and R. D. Dismuke, Phys. Rev. **170**, 37 (1968).

[50] J. Bang and J. M. Hansteen, K. Dan. Vidensk. Selsk. Mat. Fys. Medd. **31**, No. 13 (1959).

[51] J. H. Scofield, At. Data Nucl. Data Tables **14**, 21 (1974).

[52] T. Ludziejewski *et al.*, Phys. Rev. A **54**, 232 (1996).

[53] B. K. Agarwal, X-Ray Spectroscopy, edited by D. L. Mac-Adam, Springer Series in Optical Sciences Vol. 15 (Springer-Verlag, Berlin, 1979).

[54] I. Török *et al.*, Nucl. Instrum. Methods Phys. Res. B **114**, 9 (1996).

[55] T. Åberg and J. Utriainen, Phys. Rev. Lett. **22**, 1346 (1969).

[56] J. H. Scofield, Phys. Rev. A **9**, 1041 (1974).

[57] E. Storm and H. I. Israel, At. Data Nucl. Data Tables **7**, 565 (1970).